doi:10.1038/nature11877

1 Observations

1.1 Photometry and spectroscopy

On 2010 Aug. 25, the Palomar Transient Factory (PTF; Law et al. 2009; Rau et al. 2009) discovered with an autonomous machine-learning framework (Bloom et al. 2011) the Type IIn SN 2010mc (PTF 10tel; Ofek et al. 2012c) in images obtained on 2010 Aug. 20.22 UT. Further inspection of the images generated by the automatic image-subtraction pipeline revealed that the object was detected even on Aug. 20.22 (i.e., the discovery date).

We reanalysed the images using a careful image-subtraction pipeline. The improved reduction clearly shows a variable source at the location of the SN prior to the discovery date. Table 1 presents the photometric measurements of SN 2010mc, including observations made with the Oschin Schmidt 48-inch telescope, the Palomar 60-inch telescope (Cenko et al. 2006), and the *Swift*-UVOT (Gehrels et al. 2004). We note that the ground-based observations were processed using image subtraction.

A version of the light curve showing the late-time observations of the SN is presented in SI Figure 1.

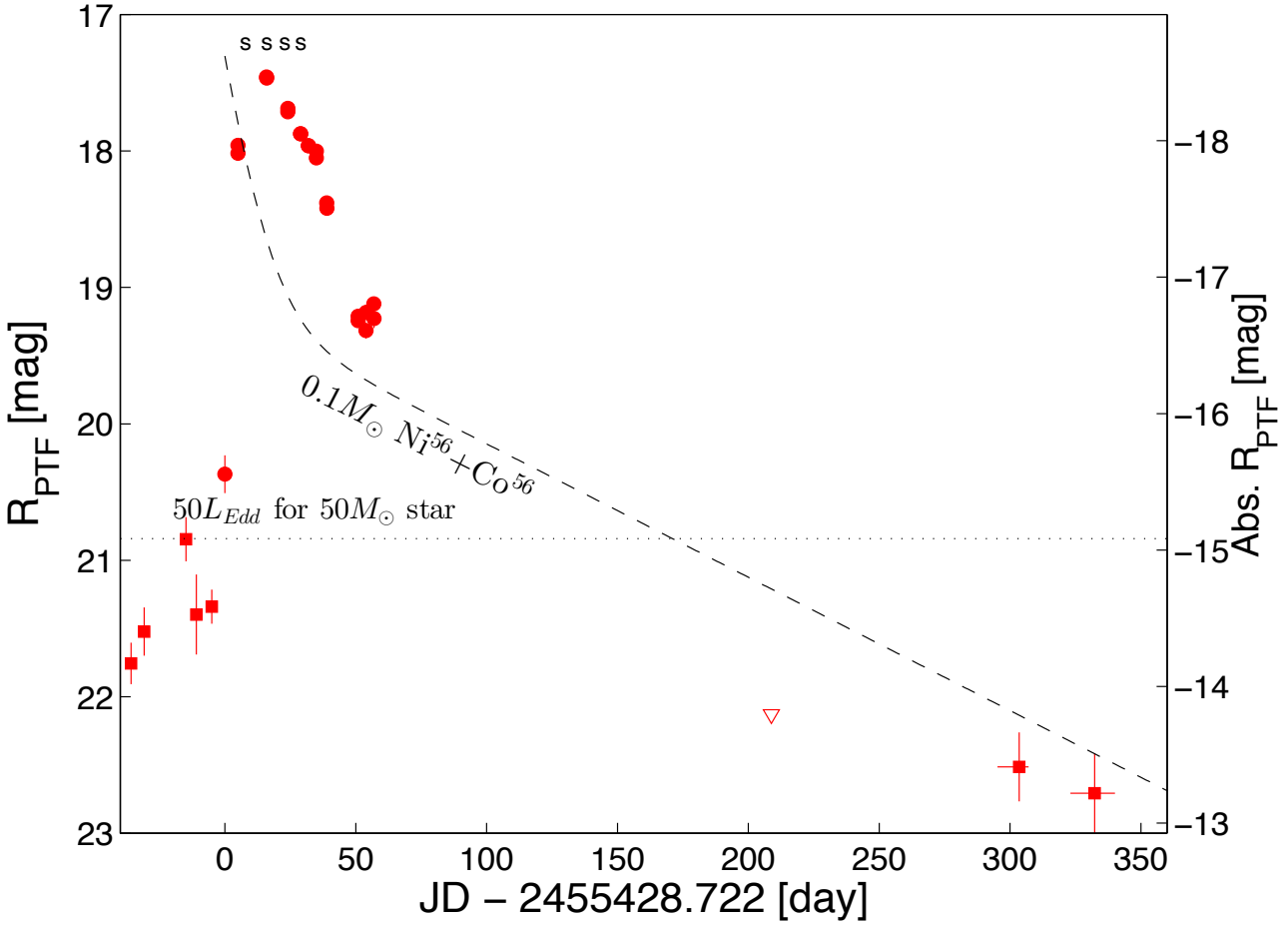

Figure 1. The light curve of SN 2010mc (PTF 10tel) as obtained with the Palomar 48-inch telescope, including late-time observations. See main text Figure 1 for details.

Telescope	Band	Time (day)	Δ_- (day)	Δ_+ (day)	N	AB Mag (mag)	Err (mag)	Mag limit (mag)
PTF	R	-0.0000	—	—	1	20.42	0.14	21.46
PTF	R	4.9600	—	—	1	18.07	0.02	21.34
PTF	R	5.0030	—	—	1	18.02	0.02	21.17
PTF	R	15.9350	—	—	1	17.50	0.01	21.05
PTF	R	15.9820	—	—	1	17.54	0.01	21.22
PTF	R	24.0140	—	—	1	17.77	0.01	21.32
PTF	R	24.0580	—	—	1	17.75	0.02	20.93
PTF	R	28.9200	—	—	1	17.91	0.01	21.54
PTF	R	28.9640	—	—	1	17.91	0.01	21.47
PTF	R	31.9190	—	—	1	17.99	0.02	21.42
PTF	R	31.9770	—	—	1	18.04	0.02	21.26
PTF	R	34.9320	—	—	1	18.14	0.02	21.43
PTF	R	34.9760	—	—	1	18.12	0.04	20.59
PTF	R	38.9240	—	—	1	18.45	0.03	21.20
PTF	R	38.9670	—	—	1	18.48	0.04	21.01
PTF	R	50.8910	—	—	1	19.34	0.03	22.07
PTF	R	50.9350	—	—	1	19.28	0.03	21.84
PTF	R	53.9120	—	—	1	19.40	0.06	21.39
PTF	R	53.9570	—	—	1	19.25	0.05	21.40
PTF	R	56.9350	—	—	1	19.16	0.04	21.58
PTF	R	56.9790	—	—	1	19.30	0.07	21.12
PTF	R	-35.8710	—	—	1	21.74	0.21	22.32
PTF	R	-35.8260	—	—	1	21.71	0.20	22.35
PTF	R	-30.8300	—	—	1	21.49	0.18	22.23
PTF	R	-14.8740	—	—	1	20.98	0.18	21.72
PTF	R	-5.0370	—	—	1	21.45	0.24	21.90
PTF	R	-4.9930	—	—	1	21.27	0.13	22.38
PTF	R	-35.8485	0.0225	0.0225	2	21.73	0.15	22.71
PTF	R	-30.8300	0.0000	0.0000	1	21.49	0.18	22.23
PTF	R	-14.8520	0.0220	0.0220	2	20.91	0.15	21.85
PTF	R	-10.9125	0.0225	0.0225	2	21.45	0.29	21.69
PTF	R	-5.0150	0.0220	0.0220	2	21.32	0.11	22.57
PTF	R	303.5230	8.3140	3.5980	5	22.44	0.23	22.93
PTF	R	332.5799	9.5219	7.5501	10	22.64	0.28	22.92
PTF	R	-125.7380	21.9790	11.0110	3	—	—	22.43
PTF	R	-96.3635	12.5635	13.5765	11	—	—	23.48
PTF	R	-70.3692	7.4648	8.5832	12	—	—	23.65
PTF	R	-67.7174	10.1166	15.9324	14	—	—	23.67
PTF	R	-60.1392	6.6858	8.3542	6	—	—	23.27
PTF	R	-51.8065	0.0215	0.0215	2	—	—	21.99
PTF	R	-51.8065	0.0215	0.0215	2	—	—	21.99
PTF	R	-46.7715	0.0225	0.0225	2	—	—	22.13
PTF	R	-40.9400	0.0000	0.0000	1	—	—	21.39
PTF	R	208.7957	1.5128	1.5122	4	—	—	22.19
PTF	R	355.6692	4.6512	6.3248	6	—	—	23.16
PTF	R	387.0123	4.0043	7.9167	3	—	—	22.48
PTF	R	419.9272	4.0323	4.0317	4	—	—	22.43

P60	g	5.9400	—	—	1	17.96	0.18	—
P60	g	7.9630	—	—	1	17.89	0.17	—
P60	g	10.0990	—	—	1	17.78	0.17	—
P60	g	10.1030	—	—	1	17.78	0.15	—
P60	g	14.0070	—	—	1	17.70	0.20	—
P60	g	15.0140	—	—	1	17.62	0.17	—
P60	g	16.0330	—	—	1	17.61	0.21	—
P60	g	17.0640	—	—	1	17.59	0.21	—
P60	g	18.0750	—	—	1	17.60	0.23	—
P60	g	19.0210	—	—	1	17.74	0.17	—
P60	g	20.0700	—	—	1	17.75	0.19	—
P60	g	21.9430	—	—	1	17.69	0.22	—
P60	g	23.0360	—	—	1	17.86	0.22	—
P60	g	32.0150	—	—	1	18.30	0.22	—
P60	g	34.9860	—	—	1	18.56	0.22	—
P60	g	40.9780	—	—	1	19.04	0.48	—
P60	g	49.9340	—	—	1	19.91	0.49	—
P60	g	50.9070	—	—	1	19.85	0.47	—
P60	g	51.9660	—	—	1	19.62	0.67	—
P60	g	52.9400	—	—	1	19.59	0.62	—
P60	g	53.9140	—	—	1	19.95	0.53	—
P60	g	55.9820	—	—	1	19.80	0.38	—
P60	g	56.9000	—	—	1	19.68	0.52	—
P60	g	69.9530	—	—	1	20.42	0.37	—
P60	g	72.8890	—	—	1	20.23	0.61	—
P60	r	7.9610	—	—	1	18.08	0.14	—
P60	r	10.0960	—	—	1	17.97	0.17	—
P60	r	10.1010	—	—	1	18.00	0.17	—
P60	r	14.0060	—	—	1	17.93	0.15	—
P60	r	15.0130	—	—	1	17.78	0.15	—
P60	r	16.0320	—	—	1	17.84	0.16	—
P60	r	17.0630	—	—	1	17.80	0.14	—
P60	r	18.0740	—	—	1	17.84	0.14	—
P60	r	19.0200	—	—	1	17.88	0.14	—
P60	r	20.0690	—	—	1	17.82	0.15	—
P60	r	21.9420	—	—	1	17.77	0.15	—
P60	r	23.0350	—	—	1	17.88	0.15	—
P60	r	32.0140	—	—	1	18.33	0.14	—
P60	r	34.0740	—	—	1	18.39	0.16	—
P60	r	49.9320	—	—	1	19.57	0.15	—
P60	r	51.9640	—	—	1	19.49	0.26	—
P60	r	53.9130	—	—	1	19.56	0.21	—
P60	r	55.9800	—	—	1	19.34	0.27	—
P60	r	72.8870	—	—	1	20.08	0.21	—
P60	i	7.9590	—	—	1	18.33	0.16	—
P60	i	10.0950	—	—	1	18.07	0.19	—
P60	i	10.1000	—	—	1	18.28	0.16	—
P60	i	14.0010	—	—	1	18.24	0.17	—
P60	i	15.0120	—	—	1	18.02	0.16	—
P60	i	16.0310	—	—	1	18.08	0.14	—
P60	i	17.0620	—	—	1	18.00	0.16	—

P60	i	18.0730	—	—	1	17.98	0.15	—
P60	i	19.0190	—	—	1	18.10	0.18	—
P60	i	20.0580	—	—	1	18.01	0.19	—
P60	i	21.9410	—	—	1	17.88	0.18	—
P60	i	23.0230	—	—	1	17.91	0.16	—
P60	i	32.0130	—	—	1	18.52	0.11	—
P60	i	34.0720	—	—	1	18.52	0.14	—
P60	i	49.9310	—	—	1	19.59	0.13	—
P60	i	53.9110	—	—	1	19.56	0.15	—
P60	i	55.9790	—	—	1	19.28	0.14	—
P60	i	68.9290	—	—	1	19.25	0.15	—
P60	i	74.9270	—	—	1	19.20	0.14	—
Swift/UVOT	UVW1	—	—	1	6.753	17.59	0.05	—
Swift/UVOT	UVW2	—	—	1	6.738	17.67	0.03	—
Swift/UVOT	UVW1	—	—	1	11.174	17.69	0.04	—
Swift/UVOT	UVW2	—	—	1	11.167	17.87	0.04	—
Swift/UVOT	UVW1	—	—	1	691.08	21.05	0.10	—
Swift/UVOT	U	—	—	1	691.88	20.54	0.08	—

Table 1: SN 2010mc (PTF 10tel) photometric measurements. Time is measured relative to JD = 2,455,428.722 day. Δ_- and Δ_+ are the lower and upper time range in which the photometry was obtained. These columns are indicated in cases where we coadded data from several images. N is the number of images. PTF magnitudes are given in the PTF magnitude system (Ofek et al. 2012a; Ofek et al. 2012b). The *Swift*/UVOT measurements represents the aperture magnitude at the position of the SN and include the host-galaxy light. The two last UVOT measurements were taken at late times; thus, they can be regarded as the magnitudes of the host galaxy. Based on them, we conclude that in order to correct the early-time measurements for the host-galaxy contamination, about 0.05 mag should be added to the SN magnitudes.

UT Date	Telescope	Instrument	Hα flux ($\mathrm{erg\,cm^{-2}\,s^{-1}}$)	broad Hα vel. ($\mathrm{km\,s^{-1}}$)	narrow Hα vel. ($\mathrm{km\,s^{-1}}$)
2010 Aug. 26	Gemini	GMOS	9.2×10^{-15}	3400	800
2010 Sep. 03	Lick	Kast	1.2×10^{-14}	1100	160
2010 Sep. 10	KPNO	RC spectrograph	9.2×10^{-15}	670	110
2010 Sep. 16	Lick	Kast	1.4×10^{-14}	4000	230

Table 2. Log of spectroscopic observations of SN 2010mc (PTF 10tel) and properties of the Hα emission line. The fluxes and velocities were measured by fitting two-component Gaussians which were convolved with the instrumental broadening as estimated from atmospheric emission lines.

In addition, we obtained spectra of SN 2010mc on four epochs, as listed in Table 2 and presented in Figure 2 of the main paper and SI Figure 2. In order to measure the line fluxes in a consistent way, we first calibrated the flux of each spectrum such that the synthetic $R_{\rm PTF}$ magnitude derived from the spectrum was identical to the $R_{\rm PTF}$ magnitude, interpolated to the epoch of each spectrum, from the PTF magnitudes listed in Table 1. All of the spectra are available online from the WISeREP website* (Yaron & Gal-Yam 2012). Each spectrum was smoothed using a median filter and a black-body curve was fitted. The derived effective temperatures and radii are presented in SI Figure 3.

The X-ray observations of PTF 10tel are presented and discussed in Section 3.

2 Derivation of mass loss as a function of the Hα line luminosity

Here we derive a relation between the mass in the circumstellar matter (CSM), the Hα emission-line luminosity $L_{\rm H\alpha}$, and the radius r. We assume that the CSM has a wind-density profile of the form $\rho = Kr^{-2}$, where $K \equiv \dot{M}/(4\pi v_{\rm w})$, $\dot{M}$ is the mass-loss rate, and $v_{\rm w}$ is the wind/outburst velocity. In this case the particle density profile is given by (e.g., Ofek et al. 2012c)

$$\begin{aligned} n &\approx \frac{1}{\langle\mu_{\rm p}\rangle}\frac{\dot{M}}{4\pi m_{\rm p} v_{\rm w} r^2} \\ &\approx 3.02\times10^{11}\frac{1}{\langle\mu_{\rm p}\rangle}\frac{\dot{M}}{0.1\,{\rm M_\odot\,yr^{-1}}}\left(\frac{v_{\rm w}}{10\,{\rm km\,s^{-1}}}\right)^{-1}\left(\frac{r}{10^{15}\,{\rm cm}}\right)^{-2}{\rm cm^{-3}}, \end{aligned} \quad (1)$$

*http://www.weizmann.ac.il/astrophysics/wiserep/; Weizmann Interactive Supernova (data) REPository.

where $\langle \mu_{\rm p} \rangle$ is the mean number of nucleons per particle (mean molecular weight). For our order-of-magnitude calculation, we adopt $\langle \mu_{\rm p} \rangle = 0.6$. Assuming the SN radiation field can ionise all of the hydrogen in the CSM, the mass of the hydrogen generating the Hα line is

$$M_{\rm H} \approx \frac{m_{\rm p} L_{\rm H\alpha}}{h \nu_{\rm H\alpha} \alpha^{\rm eff}_{\rm H\alpha} n_{\rm e}}. \quad (2)$$

Here $\nu_{\rm H\alpha}$ is the Hα frequency (4.57×10^{14} Hz), $\alpha^{\rm eff}_{\rm H\alpha}$ is the Hα effective recombination coefficient, $\sim 8.7 \times 10^{-14} T_{\rm 10k}^{-0.89}$ cm^3 s^{-1} (Osterbrock & Ferland 2006), where $T_{\rm 10k}$ is the temperature in units of 10,000 K. We assume $T_{\rm 10k} = 1$. In a wind profile, the integrated mass from radius r_0 to r is

$$M = \int_{r_0}^{r} 4\pi r^2 K r^{-2} dr = 4\pi K (r - r_0) \approx 4\pi K r, \quad (3)$$

where the last step assumes that $r_0 \ll r$. By substituting Equation 1 into Equation 2 and setting it equal to Equation 3, we can get a relation between the mass-loading parameter K, the Hα luminosity, and the radius:

$$\begin{aligned} K &\gtrsim \left(\frac{\langle \mu_{\rm p} \rangle m_{\rm p}^2 L_{\rm H\alpha} r}{4\pi h \nu \alpha^{\rm eff}} \right)^{1/2} \\ &\approx 7.1 \times 10^{15} \left(\frac{L_{\rm H\alpha}}{10^{41}\,{\rm erg\,s^{-1}}} \right)^{1/2} \left(\frac{r}{10^{15}\,{\rm cm}} \right)^{1/2} {\rm g\,cm^{-1}}. \end{aligned} \quad (4)$$

The reason for the inequality is that in practice, it is possible that not all of the hydrogen is ionised or that the temperature of the gas is too high (i.e., $\alpha^{\rm eff}_{\rm H\alpha}$ depends on temperature).

Assuming the outburst ejected material with a velocity of 2000 km s^{-1} at day -37, then at the time the first spectrum was taken (day 6), the ejecta radius is $r \approx 7 \times 10^{14}$ cm. This radius is consistent with the one derived from the black-body fit to the spectrum at the first epoch (see SI Figure 3). Using the measured flux of the Hα broad component at day 6 (9×10^{-15} erg cm^{-2} s^{-1}; Table 2), the luminosity of the Hα broad component is $\sim 3 \times 10^{40}$ erg s^{-1}. Substituting these values into Equation 4, and assuming a wind velocity of 2000 km s^{-1}, we find a mass-loss rate of $\gtrsim 10^{-1}$ M$_\odot$ yr^{-1}. Assuming a one month long outburst this gives a total mass of about 10^{-2} M$_\odot$. This value is in excellent agreement with the mass-loss rate we independently find based on the kinetic-energy arguments and the diffusion time scale.

We note that this derivation assumes that the narrow lines are due to the interaction of the CSM with the SN radiation field. One caveat, is that it is possible that some, or all,

UT Date	Time since disc. (day)	Exp. Time (s)	2σ upper limit ($\mathrm{ct\,ks^{-1}}$)
2010 Aug. 27.0	6.8	1342	2.2
2010 Aug. 31.4	11.2	2256	1.3
2012 July 11.7	691.5	4818	0.62

Table 3. *Swift*-XRT observations of SN 2010mc (PTF 10tel).

of the line flux originates from a shock interaction or from a slow moving ejecta. However, the order of magnitude consistency between this mass-loss estimate and other mass-loss estimators suggest that such an effect is not significant.

3 X-ray observations

The *Swift*-XRT observations of SN 2010mc (PTF 10tel) in the 0.2–10 keV band are listed in Table 3. For each *Swift*-XRT image of the SN, we extracted the number of X-ray counts in the 0.2–10 keV band within an aperture of 7.2″ (3 pixels) radius centred on the SN position. We chose a small aperture in order to minimise any host-galaxy contamination. We note that this aperture contains $\sim 37\%$ of the source flux (Moretti et al. 2004). The background count rates were estimated in annuli around each SN, with an inner (outer) radius of 50″ (100″). Assuming a photon spectrum $n_{\rm ph} \propto E^{-\Gamma}$ with $\Gamma = 2$, a Galactic neutral hydrogen column density of $2.34 \times 10^{20}\,\mathrm{cm^{-2}}$ in the direction of the SN (Dickey & Lockman 1990), and correcting for the photometric aperture losses, we find a 2σ upper limit on the luminosity in the second epoch of $3.5 \times 10^{41}\,\mathrm{erg\,s^{-1}}$.

Following Immler et al. (2008), the X-ray emission from the optically thin region is given by

$$L_{\rm X} \approx \int_r^{\infty} 4\pi r^2 \Lambda(T) n^2 dr, \qquad (5)$$

where $\Lambda(T)$ is the effective cooling function in the 0.2–10 keV range. Assuming an optically thin thermal plasma with a temperature in the range 10^6–10^8 K (Raymond et al. 1976), we adopt a value of $\Lambda(T) \approx 3 \times 10^{-23}\,\mathrm{erg\,cm^3\,s^{-1}}$. Substituting Equation 1 into Equation 5 we get

$$L_{\rm X} \approx 4\pi\Lambda(T)\frac{K^2}{\langle\mu_{\rm p}\rangle^2 m_{\rm p}^2 r}$$

$$\approx \quad 2.4\times10^{40}\left(\frac{\dot{M}}{0.01\,\mathrm{M_\odot\,yr^{-1}}}\right)^{2}\left(\frac{v_w}{2000\,\mathrm{km\,s^{-1}}}\right)^{-2}\left(\frac{r}{10^{15}\,\mathrm{cm}}\right)^{-1}\mathrm{e}^{-(\tau+\tau_{\rm bf})}\,\mathrm{erg\,s^{-1}}. \quad (6)$$

Here, we added a correction factor due to absorption in the wind, where τ and $\tau_{\rm bf}$ are the Thomson and bound-free optical depths, respectively. In our case the Thomson optical depth will be 1 for $\dot{M}\approx0.1\,\mathrm{M_\odot\,yr^{-1}}$ (e.g., Ofek et al. 2012c). Although the Thomson optical depth is well known, when the optical depth is of the order of a few, Compton scattering is expected to reprocess more energetic photons into the 0.2–10 keV band (Chevalier & Irwin 2012; Svirski et al. 2012). Since the exact X-ray spectrum is not known (Katz et al. 2011; Svirski et al. 2012), a proper calculation of $L_{\rm X}$ when $\tau\gtrsim1$ is not straightforward. Regarding the bound-free optical depth, although it is likely that all the hydrogen is ionised, Chevalier & Irwin (2012) argued that if the shock velocity is below $\sim10^4\,\mathrm{km\,s^{-1}}$ some of the metals will be neutral. In this case bound-free absorption will be important and it is given by (Ofek et al. 2012c)

$$\tau_{\rm bf}\approx15\left(\frac{\dot{M}}{0.01\,\mathrm{M_\odot\,yr^{-1}}}\right)\left(\frac{v_{\rm w}}{2000\,\mathrm{km\,s^{-1}}}\right)^{-1}\left(\frac{r}{10^{15}\,\mathrm{cm}}\right)^{-1}\left(\frac{E_{\rm X}}{1\,\mathrm{keV}}\right)^{-2.5}, \quad (7)$$

where $E_{\rm X}$ is the X-ray energy.

If we ignore the Thomson optical depth (i.e., $\tau=0$), and if we assume a flat spectrum (i.e., constant number of photons per unit energy) and the *Swift*-XRT spectral response, from Equations 6 and 7 we find that the mass-loss rate is either smaller than about $0.1\,\mathrm{M_\odot\,yr^{-1}}$ or larger than about $1\,\mathrm{M_\odot\,yr^{-1}}$. The low bound of $\dot{M}\lesssim0.1\,\mathrm{M_\odot\,yr^{-1}}$ is consistent with the other mass-loss estimates.

4 Radio observations

We observed SN 2010mc (PTF 10tel) with the Jansky Very Large Array (JVLA[†]) on 2012 Sep. 10, about two years after the SN discovery. The observation was undertaken in the K band (21.8 GHz). We used J1727+4530 for phase calibration and 3C 286 for flux calibration. The data were reduced using the AIPS software. We did not detect SN 2010mc with an upper limit of 0.2 mJy (3σ).

[†]The Jansky Very Large Array is operated by the National Radio Astronomy Observatory (NRAO), a facility of the National Science Foundation operated under cooperative agreement by Associated Universities, Inc.

5 Diffusion time scale limit on mass loss

Another observable that can be used to constrain the mass in the CSM is the rise time of the SN light curve. If a considerable amount of material is present between the SN and the observer, then photon diffusion will slow down the rise time of the SN light curve. Therefore, the maximum observed SN rise time can be used to put an upper limit on the amount of mass between the SN and the observer. The diffusion time scale in a wind profile is given by (e.g., Ginzburg et al. 2012)

$$\begin{aligned} t_{\rm diff} &\approx \frac{\kappa K}{c}[\ln\left(\frac{c}{v_{\rm sh}}\right) - 1] \\ &\approx 0.08\left(\frac{\kappa}{0.34\,{\rm cm^2\,gr^{-1}}}\right)\left(\frac{\dot{M}}{10^{-2}\,{\rm M_\odot\,yr^{-1}}}\right)\left(\frac{v_{\rm w}}{2000}\right)^{-1}\left[\ln\left(30\frac{v_{\rm ej}}{10^4\,{\rm km\,s^{-1}}}\right) - 1\right]\,{\rm day} \end{aligned} \quad (8)$$

Here $v_{\rm ej}$ is the SN shock velocity. In our case, assuming the rise time of the SN is about seven days, we can use Equation 8 to set an upper limit, $\dot{M} < 0.4\,{\rm M_\odot\,yr^{-1}}$.

6 Alternative interpretations

Here we consider alternative interpretations regarding the nature of the precursor bump and show that they are not consistent with the observations. One possibility is that this feature is due to a shock breakout (e.g., Colgate 1974) prior to the SN rise. However, given the feature's luminosity, its duration is at least an order of magnitude too long to be consistent with a shock breakout (e.g., Nakar & Sari 2010; Rabinak & Waxman 2011).

A second possibility is that the first bump represents a SN explosion while the second peak is due to the interaction of the SN ejecta with dense CSM and the conversion of the SN kinetic energy into radiated luminosity. However, this scenario can be rejected based on the fact that by fitting a black-body spectrum to the spectra (see SI Figure 3), we can find the temperature and photospheric radius evolution between days 5 and 27. These fits suggest that the photosphere is expanding with a mean velocity of $\gtrsim$4300 km s^{-1}, and that the black-body radius at day 6 is $\sim 6 \times 10^{14}$ cm. Extrapolating backward, this suggests that the SN outburst happened after day -10.

Another argument against this scenario is that the SN spectrum at day 27 after discovery (main text Figure 2), shows a P-Cygni profile with a velocity of $\sim 10^4\,{\rm km\,s^{-1}}$. At the same time, the black-body radius of the SN photosphere is $\sim 1.5 \times 10^{15}$ cm. These values

are roughly consistent (to within 30%) with an explosion time at day 0, and are less consistent with explosion at day −37 day relative to discovery. A caveat in this statement is that the photospheric radius which controls the black-body temperature of the continuum is not necessarily at the same position where the P-Cygni absorption is generated.

7 The Type Ibn SN 2006jc

Another possibly related event is SN 2006jc (Nakano et al. 2006). Unlike SN 2010mc (PTF 10tel) and SN 2009ip, this was a hydrogen-stripped Type Ibn SN. In this case an optical outburst was observed in 2004, about two years prior to the SN explosion (Nakano et al. 2006), creating a dense circumstellar shell (Foley et al. 2007; Immler et al. 2008; Smith et al. 2008; Ofek et al. 2012c). Foley et al. (2007) suggested that the progenitor was a Wolf-Rayet star that had an outburst two years prior to its explosion, creating the CSM; it may have recently transitioned from the LBV phase. However, Pastorello et al. (2007) argued that SN 2006jc took place in a binary system in which one star (a Wolf-Rayet star) was responsible for the SN explosion while the companion was a luminous blue variable (LBV) that generated the eruption in 2004. Our argument regarding the causality between pre-explosion outbursts and the SN explosions disfavours the explanation given by Pastorello et al. (2007) for SN 2006jc. However, for SN 2006jc, the time difference between the precursor event and the explosion is about two years (rather than one month), rendering the argument a factor ~ 20 weaker than in the case of PTF 10tel.

8 The probability of detecting a precursor outburst prior to the explosion

The specific precursor event reported in this paper was found as a part of a search for outbursts among type-IIn SN in PTF data. The sample we used included only four nearby type-IIn SNe with good pre-explosion coverage. Nevertheless, in estimating the probability of detecting a precursor prior to the explosion we assumed a sample size of 20 (five times higher than our actual sample size), accounting for other samples in which outburst events could have been detected (see details below). This sample size thus facilitates a conservative rate estimate.

Thus far the brightest precursor outbursts (e.g., PTF 10tel) have an absolute magnitude

of about −16. Using previous-generation transient surveys, such bursts can be detected up to a distance of ∼ 100 Mpc, while the new-generation surveys (e.g., PTF) may be able to detect them to somewhat larger distances. Among the 165 SNe IIn listed in the IAUC website, about 70 have distances below 100 Mpc. Many of these SNe were found using small telescopes which are limited by their depth. Based on the PTF experience, we estimate that not more than 20% of these SNe have sufficiently good pre-explosion observations that will allow the detection of a precursor prior to the explosion. In addition, PTF has already found 91 SNe IIn (some listed in the IAUC website), of which only a few are sufficiently nearby, and have high cadence and almost continuous observations prior to the explosion. Thus, we conclude that up to 20 SNe IIn discovered so far have good enough pre-explosion observations to find precursor outbursts.

We note that even if we assume that *all* of the ∼ 250 SNe IIn discovered so far have sufficiently good observations prior to the SN explosion, this will not change our conclusion that precursor outbursts are more common, or are causally connected with the final stages of massive-star evolution.

Finally, we note that we cannot completely rule out the possibility that the SN and precursor are two unrelated events (e.g., explosions of two different stars in a star cluster). However, we think this is an unlikely possibility given the evidences presented in this paper, including consistency of the mass-loss estimators with the properties of the outburst (luminosity and time before SN), and the small number of type-IIn SNe in which we searched for precursor events.

9 Theoretical determination of the precursor mass loss

The precursor is characterised by a rapid brightening of the radiative flux which is sustained at a highly super-Eddington level for a month. The relatively short time scales imply that some efficient mechanism exists to very quickly transport the flux out, even faster than convection can. The mechanism suggested by Quataert & Shiode (2012), where the energy is transported outward by acoustic waves, offers a natural explanation. However, this mechanism can operate only in regions with a sufficiently high density. At a region where the density, ρ, satisfies $L \approx L_{\rm conv,max} \approx 4\pi r^2 \rho v_{\rm s}^3$ (where $v_{\rm s}$ is the speed of sound), the

acoustic energy flux L is converted into a radiative flux L. The mass-loss rate expected in such a case is $\dot{M} \approx 4\pi r^2 \rho v_s \approx L/v_s^2$. Assuming $v_s \approx 60\,\mathrm{km\,s^{-1}}$ at the base of the wind gives roughly $8\,\mathrm{M}_\odot$ for the mass ejected during the precursor. A similar problem exists for the great (super-Eddington) eruption of η Carina. The naive expectation for the mass loss is orders of magnitude larger than what was actually observed (Shaviv 2000).

To overcome this discrepancy, it was suggested that instabilities reduce the effective opacity of super-Eddington atmospheres. This implies that a wind is accelerated only from lower-density regions where a typical scale height in the atmosphere becomes of order unity and the effective opacity returns to its microscopic value. Under these assumptions, the mass-loss was determined by Shaviv (2001) to be $\Delta M = W \Delta T (L - L_{\mathrm{Edd}})/(c v_s)$, where ΔT is the duration of the outburst and L is the luminosity at the base of the wind (where part of the latter is converted into mechanical energy of the mass loss). W is a dimensionless constant which depends on the geometry of the instabilities, and empirically was found to be around 3 (± 0.5 dex).

We can use this expression to predict the expected mass loss from the super-Eddington precursor. To do so we have to add the mechanical energy of the wind to the observed luminosity and obtain the total luminosity at the base of the wind. The mechanical energy itself is given by $L_{\mathrm{mech}} = \Delta M/2(v_\infty^2 + v_{\mathrm{esc}}^2)$. Here v_∞ is the terminal velocity at infinity and v_{esc} is the escape velocity. We crudely take $v_{\mathrm{esc}} \approx v_\infty$. Since the luminosity at the base is significantly super-Eddington, we can ignore the L_{Edd} term. If we further consider that $v_s \approx 30\,\mathrm{km\,s^{-1}}$, we obtain $\Delta M \approx 0.05\,\mathrm{M}_\odot$ (with an uncertainty of about 0.5 dex). This value sits comfortably in the observationally determined range of possible mass loss in SN 2010mc (PTF 10tel).

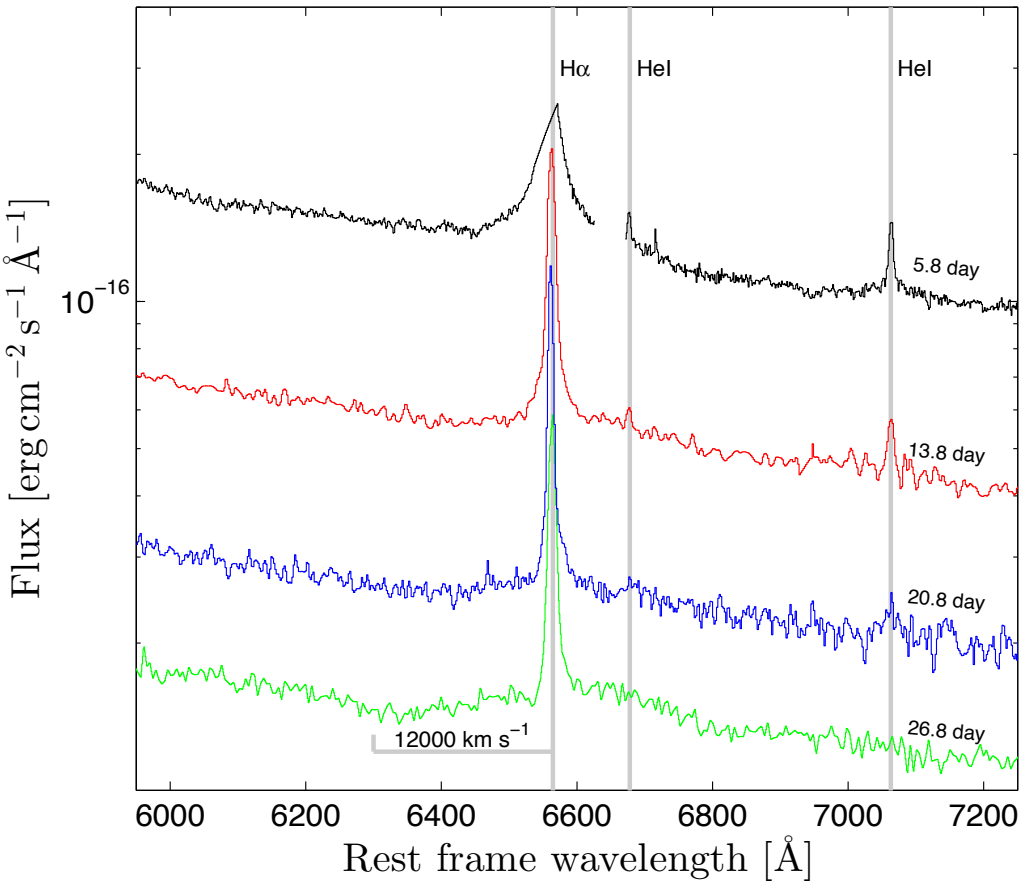

Figure 2. Close-up view of the Hα line in the spectra of SN 2010mc (PTF 10tel). The best–fit width and total flux of a two-component model at each epoch are listed in Table 2. The width of the Hα emission is decreasing significantly after the first epoch, from 3400 km s^{-1} to $\lesssim$ 1000 km s^{-1}. In the last epoch a P-Cygni profile develops, with a velocity difference between the peak of the emission and the bottom of the absorption of over 10^4 km s^{-1}. The velocity of the Hα absorption component in the P-Cygni feature is marked with a 12,000 km s^{-1} label. The P-Cygni profile is better seen in the stretch of Figure 2 (main text). Also visible is the decrease in strength of the He I lines, presumably due to the decrease in temperature (see SI Figure 3).

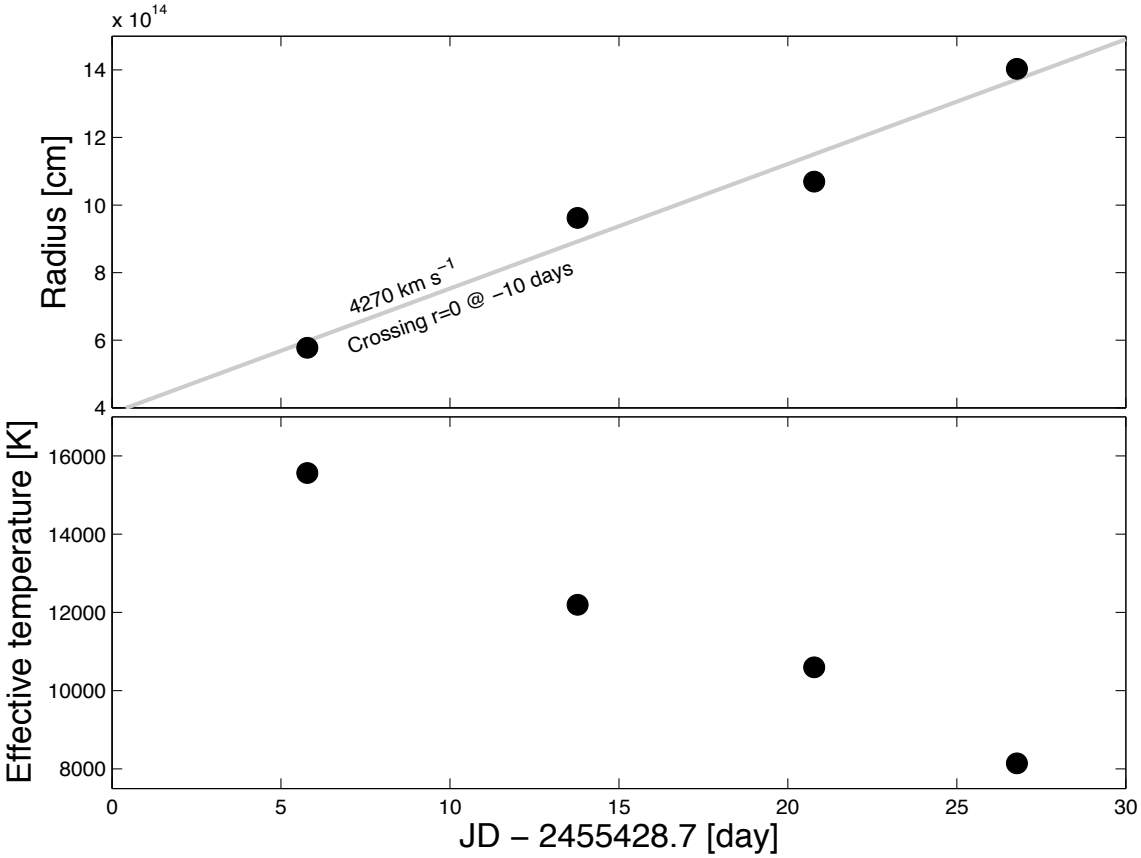

Figure 3. Black-body temperature and radius derived from the spectra of SN 2010mc (PTF 10tel). The temperature estimate should be regarded as a lower limit, because the peak of the emission is outside the optical region and metal line blanketing can reduce the flux in the blue parts of the spectrum. The reduction in temperature is consistent with the fact that the He I lines are becoming weaker at later epochs (SI Figure 2). We note that the best-fit temperature at day 6 (near the first spectroscopic observation) based on the broad-band *Swift*/UVOT and P60 photometry is about 19,000 K. The nondetection of He II lines also suggests that the temperature is not much higher than the value derived here.

Received 14 December 2012; Accepted **draft**.

30. Bloom, J. S., Richards, J. W., Nugent, P. E., et al., Automating Discovery and Classification of Transients and Variable Stars in the Synoptic Survey Era. arXiv:1106.5491 2011

31. Cenko, S. B., Fox, D. B., Dae-Sik, M., et al., The Automated Palomar 60 Inch Telescope. *PASP*, **118**, 1396-1406 (2006)

32. Chevalier, R. A., Irwin, C. M., X-Rays from Supernova Shocks in Dense Mass Loss. *ApJ*, **747**, L17 (2012)

33. Dickey, J. M., Lockman, F. J., H I in the Galaxy. *ARA&A*, 215-261 (1990)

34. Colgate, S. A., Early Gamma Rays from Supernovae. *ApJ*, **187**, 333-336 (1974)

35. Foley, R. J., Smith, N., Ganeshalingam, M., et al., SN 2006jc: A Wolf-Rayet Star Exploding in a Dense He-rich Circumstellar Medium. *ApJ*, **657**, L105-108 (2007)

36. Gehrels, N., Chincarini, G., Giommi, P., et al., The Swift Gamma-Ray Burst Mission. *ApJ*, **611**, 1005-1020 (2004)

37. Immler, S., Modjaz, M., Landsman, W., et al., Swift and Chandra Detections of Supernova 2006jc: Evidence for Interaction of the Supernova Shock with a Circumstellar Shell. *ApJ*, **674**, L85-88 (2008)

38. Katz, B., Sapir, N., Waxman, E., X-rays, gamma-rays and neutrinos from collisionless shocks in supernova wind breakouts. arXiv 1106.1898

39. Nakar, E., Sari, R., Early Supernovae Light Curves Following the Shock Breakout. *ApJ*, **725**, 904-921 (2010)

40. Quataert, E., & Shiode, J. Astrophysics of gaseous nebulae and active galactic nuclei, 2nd. ed

41. Raymond, J. C., Cox, D. P., Smith, B. W., et al., Radiative cooling of a low-density plasma. *ApJ*, **204**, 290-292 (1976)

42. Shaviv, N. J., The Porous Atmosphere of η Carinae. *ApJ*, **532**, L137-140 (2000)

43. Shaviv, N. J., The theory of steady-state super-Eddington winds and its application to novae. *MNRAS*, **326**, 126-146 (2001)

44. Svirski, G., Nakar, E., Sari, R., Optical to X-rays SNe light curves following shock breakout through a thick wind. arXiv 1202.3437

45. Rabinak, I., Waxman, E., The Early UV/Optical Emission from Core-collapse Supernovae. *ApJ*, **728**, 63 (2011)

46. Ginzburg, S., Balberg, S. Superluminous Light Curves from Supernovae Exploding in a Dense Wind. *ApJ*, **757**, 178-191 (2012)